



High resolution digital image correlation mapping of strain localization upon room and high temperature, high cycle fatigue of a TiAl intermetallic alloy



Thomas Edward James Edwards^{a,b,*}, Fabio Di Gioacchino^{a,1}, William John Clegg^a

^a Department of Materials Science and Metallurgy, 27 Charles Babbage Rd, University of Cambridge, Cambridge CB3 0FS, UK

^b Empa, Swiss Federal Laboratories for Materials Science and Technology, Laboratory for Mechanics of Materials and Nanostructures, Feuerwerkerstrasse 39, 3602 Thun, Switzerland

ARTICLE INFO

Keywords:

Titanium aluminide
High temperature fatigue
High cycle fatigue
High resolution digital image correlation strain mapping
Strain localization

ABSTRACT

Microplasticity in a lamellar TiAl alloy upon high cycle tensile fatigue was measured by high resolution digital image correlation strain mapping at several stress and cycle increments, at 25 °C and 670 °C, for two lamellar thicknesses. Plastic deformation occurred primarily in soft-mode colonies at both temperatures, operating by slip parallel to the lamellae, and near lamellar interfaces. Plastic strains generally decreased to zero by the colony boundary; strain transfer across such boundaries was rare at both temperatures. At 25 °C, the maximum applied stress influenced the number of slip bands more so than did the number of loading cycles.

1. Introduction

Gamma titanium aluminide (γ -TiAl) alloys are an emerging light-weight system capable of replacing nickel superalloys in a range of transport and energy industries [1–4], with both current applications and future ones envisaged [1]. γ -TiAl alloys are known to have poor fatigue crack growth (FCG) tolerance in comparison to competitor steels and Ni superalloys, relating to low toughness, ductility and crack growth threshold [5]. For aero-engine applications, this has led to a high cycle fatigue (HCF) lifing strategy whereby γ -TiAl alloys are maintained below 50% of the highest peak cyclic stress at which the material can endure 10^7 cycles [6]. This in turn aims to maintain stress intensity factors below the threshold for fatigue crack growth.

Lamellar γ -TiAl alloys exhibit a fourfold strength anisotropy [7]. Hence at the maximum stress where 10^7 cycles are achievable (the run-out stress), approximately 80% of the yield stress [8], the softest lamellar colonies may experience loads above their respective plastic limit. Indeed, it is not necessary to be in the presence of the crack tip stress concentration of standard FCG studies to observe plasticity when cycling well below the run-out stress. Such microplasticity in lamellar γ -TiAl alloys, e.g. longitudinal twinning and dislocation motion, may be extensive in a reduced number of colonies. It is therefore thought that during HCF of lamellar γ -TiAl, considerably heterogeneous

distributions of deformation occur, where some colonies exhibit low cycle fatigue-type plasticity levels, whilst others may remain elastic.

The method of digital image correlation (DIC), which allows the total strain of a surface to be measured upon deformation by tracking the locally differential motion of reference surface features or fiducial markers, has been applied to the γ -TiAl alloys to study low cycle fatigue (LCF) at 25 °C and 700 °C [9]. It was found that after only 20% of the total lifetime, the location of final failure was detected. Similarly, the studies of Filippini, Patriarca and collaborators [10,11] report inhomogeneities in the distribution of plastic strain at the lamellar scale, between α_2 -Ti₃Al and γ -TiAl lamellae, with lamellar orientation to the loading axis playing a key role therein. Bode et al. [12] further associate fatigue loading in their large (1500 μ m) TiAl lamellar colonies with dominant shear deformation parallel to the lamellar planes: the longitudinal deformation mode [13]. These early studies, and others, are reviewed further by the authors in [5]; a key limitation is the relatively low spatial resolution of the optical microscopy employed which stymies the interpretation of the data.

More recently, a series of studies by Edwards and co-workers [14–17] have been performed where the DIC strain mapping method was employed using the higher resolution afforded by scanning electron microscopy (SEM) to measure total strains at the sample surface upon compressive and tensile uniaxial monotonic loading of macroscopic

* Corresponding author at: Empa, Swiss Federal Laboratories for Materials Science and Technology, Laboratory for Mechanics of Materials and Nanostructures, Feuerwerkerstrasse 39, 3602 Thun, Switzerland.

E-mail addresses: thomas.edwards@empa.ch (T.E.J. Edwards), fdigioacchino@mines.edu (F. Di Gioacchino), wjc1000@cam.ac.uk (W.J. Clegg).

¹ Present address: ASPPRC, Dept. Metallurgical and Materials Engineering, Colorado School of Mines, 1500 Illinois St, Golden, CO, USA.

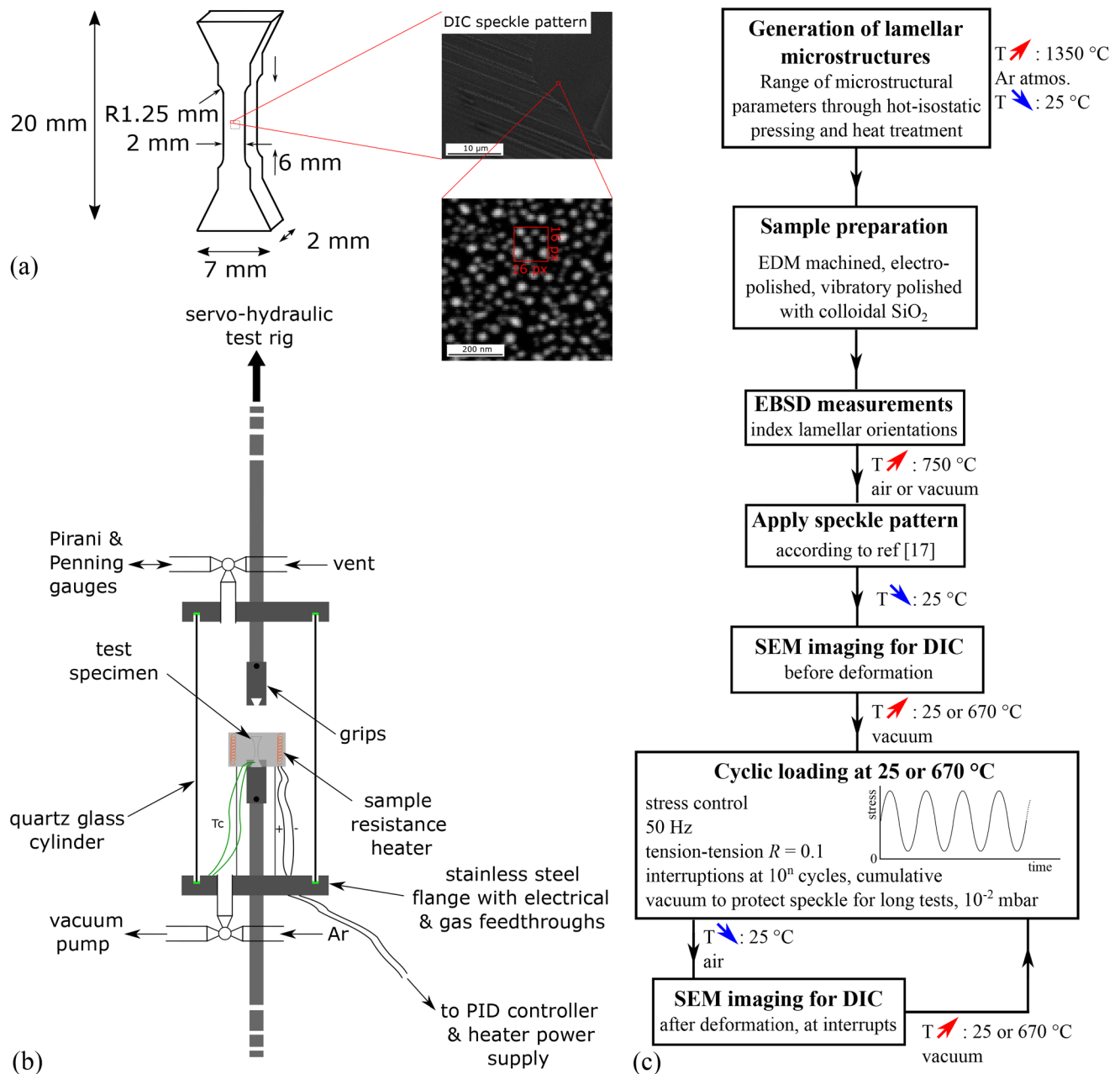


Fig. 1. (a) specimen geometry for high cycle fatigue (HCF) testing, (b) diagram of experimental chamber built for controlled atmosphere fatigue testing, adapted from [16], (c) flow chart of experimental method, from microstructure modification, through sample preparation, mechanical test execution, and strain and crystal orientation measurements, adapted from [26]. In (a) the Au reconstructed thin film speckle pattern inset is imaged with backscattered electrons, as used for DIC processing; the 16×16 px² correlation subset employed is additionally indicated.

polycrystalline lamellar γ -TiAl alloy testpieces. Furthermore, micro-compression samples constituted of single stacks of lamellae, milled from individual lamellar colonies with prescribed orientations to the loading axis, were also studied with the same method in monotonic microcompression [15,18–22]. For both sample sizes, the spatial resolution of strain mapping was of the order of 60–100 nm. Such studies identified the onset of localised plastic deformation to occur much below the yield stress, at less than 64% of the yield stress, at both 25 and 700 °C, which is the upper design temperature envisioned for second generation alloys in service, thereby confirming the above suspicions that significant amounts of localised plasticity occur well below the general yield stress. Such localised plastic deformation may play an important role in the fatigue behaviour of titanium aluminide alloys.

This paper therefore aims to characterise the spatial distribution of

plasticity occurring during tensile high cycle fatigue loading of a commercial TiAl alloy at room and high temperature, with nano-scale resolution strain mapping of microplasticity through an advanced digital image correlation technique.

2. Experimental procedures

2.1. Material and metallographic preparation

The TiAl alloy studied, Ti-45Al-2Nb-2Mn(at%)-0.8 vol% TiB_2 (Ti4522XD), presented a nearly lamellar microstructure following processing, detailed in [14]. Two microstructural conditions were produced by heat treatment: a thicker condition with a γ -TiAl lamellar thickness of 1.4 μm , and a thinner one with γ -TiAl lamellae 160 nm

Thick lamellae, 25 °C

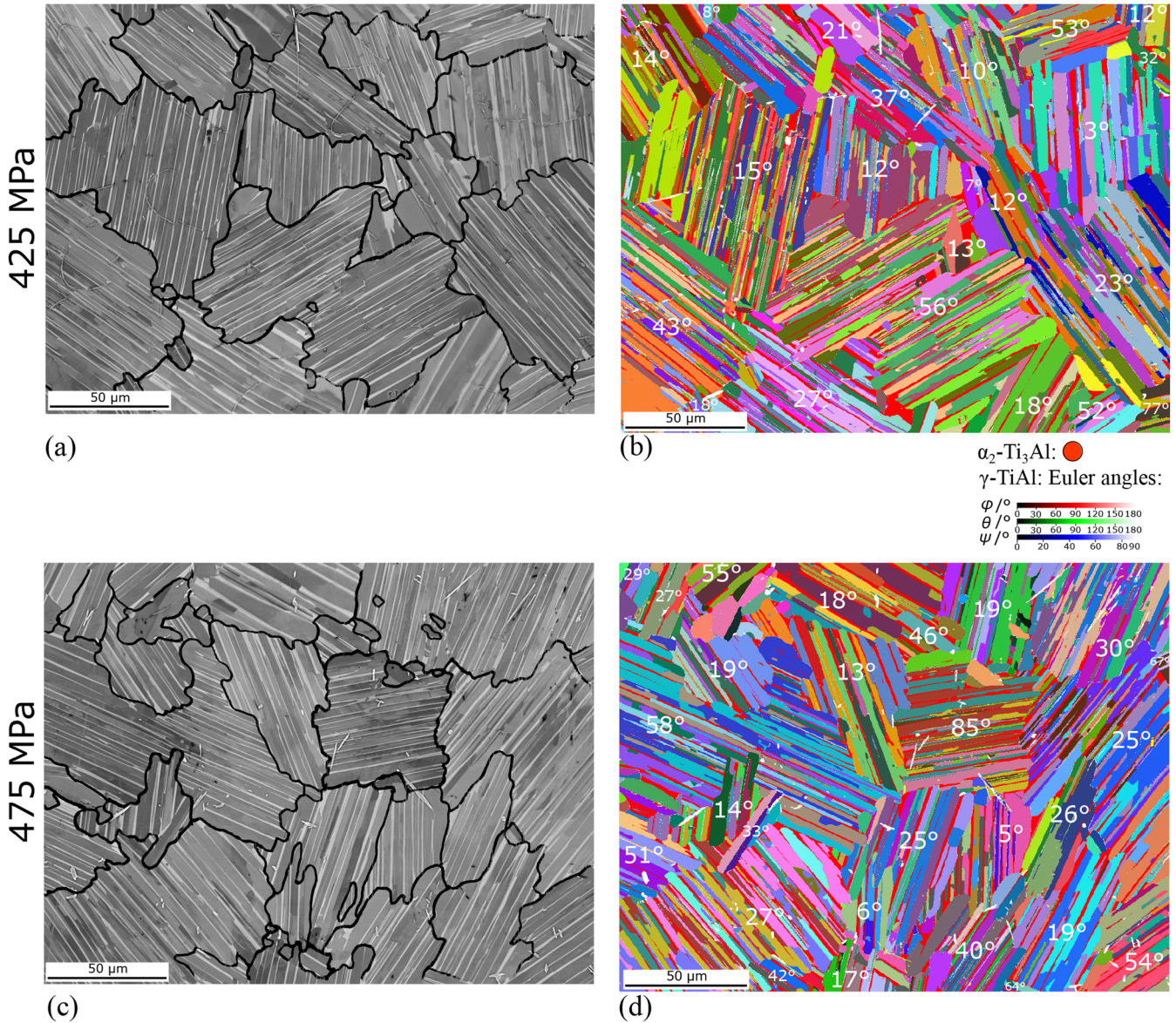


Fig. 2. Backscattered electron (BSE) and electron backscatter diffraction (EBSD) maps of the regions of interest for HCF testing of the as-HIP condition of Ti4522XD at 25 °C. The angle ϕ between the lamellar planes and the loading axis is indicated for each lamellar colony on the EBSD maps.

thick; a more complete description of the microstructural parameters of the two material conditions was given previously [14].

Test specimens with a $6 \times 2 \times 2$ mm³ gauge length, Fig. 1(a), were electro-discharge machined (EDM), first to 0.2 mm oversize, then to the correct dimensions; this mitigated any elastic relaxation of the material upon the first EDM cut that could lead to imperfect dimensions. Following this, the specimens were electropolished in a solution of 5% perchloric acid, 35% butan-1-ol, 60% methanol under a potential of 15 V. One large face was further prepared for electron backscatter diffraction (EBSD) mapping by vibratory polishing in a colloidal silica solution for 48 h. No fiducial markers were applied to any testpieces, to avoid initiating premature failure from a fiducial indent upon tensile fatigue loading, for example. EBSD mapping of regions of interest 180×230 μm² in size within the gauge length before mechanical testing, as in Fig. 2(a,b), was performed as previously [14].

2.2. Mechanical testing

High cycle fatigue testing was carried out *ex situ* on a 100 kN servo-hydraulic machine (Mayes, UK) at a frequency of 50 Hz and a stress ratio $R = 0.1$ (tension–tension) with a sinusoidal waveform. At each temperature and microstructural condition, two maximum cycling stresses, σ_{\max} , were considered: $\sigma_{\max,th}$, the threshold value for run-out (10^7 cycles) determined previously (425 MPa at 25 °C, 380 MPa at 670 °C), and $\sigma_{\max,th} + 50$ MPa. A custom-built test chamber [16], Fig. 1(b), enabled heating to above 800 °C using a resistance heater controlled against a remote thermocouple located in the Ni superalloy (Mar M002) sample grips. Initial calibration of the remote thermocouple relative to thermocouples spot-welded to the gauge of dummy samples determined the sample temperature to vary approximately sinusoidally with time with an amplitude of 1 °C. Unlike previous high temperature monotonic testing in air [14], for high temperature HCF testing, the test chamber generally operated under vacuum ($< 10^{-2}$ mbar), following three pump-purge cycles with Ar gas. This aimed to

Thick lamellae, 25 °C, 425 MPa

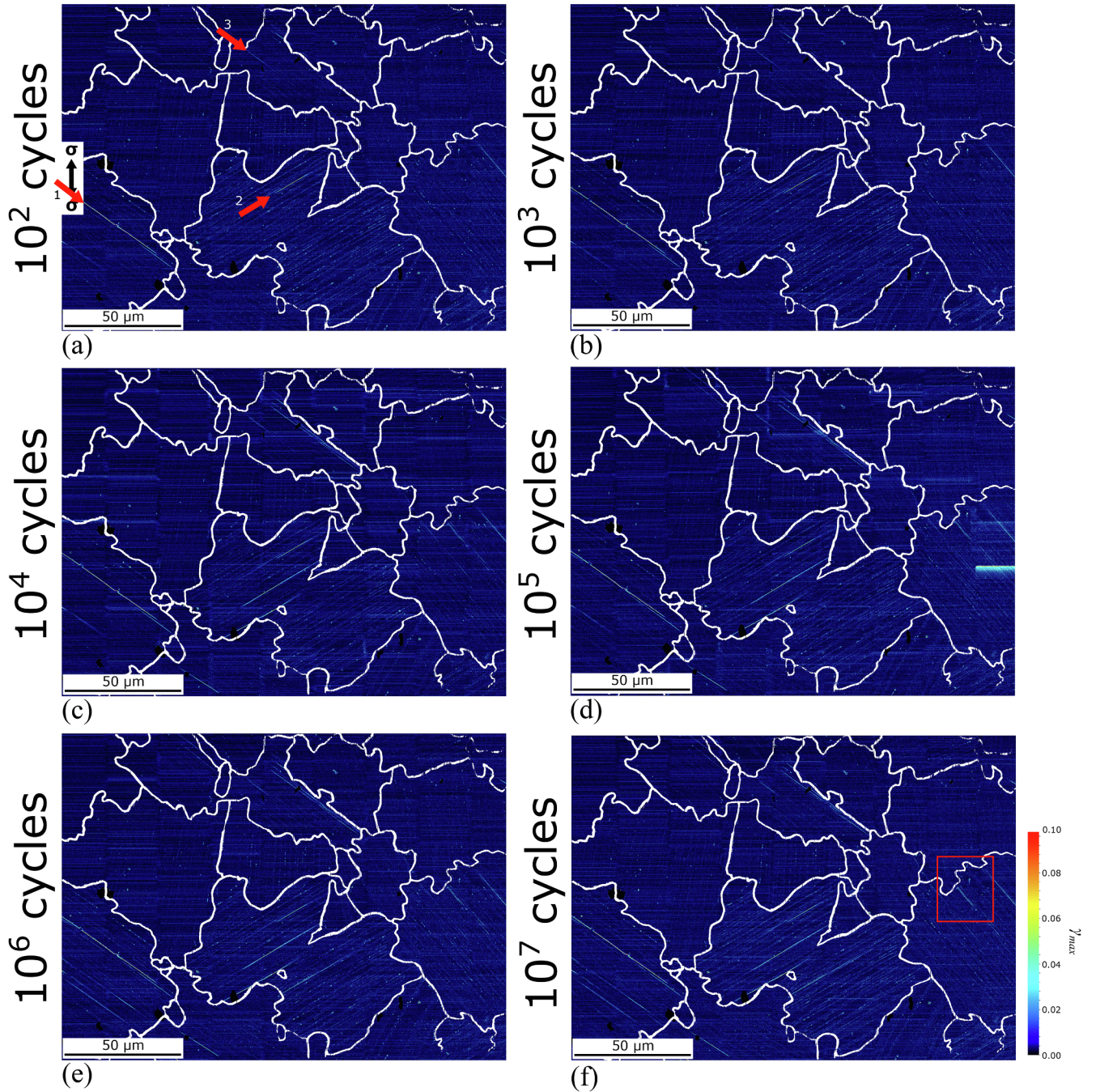


Fig. 3. Maximum shear strain maps for HCF of the as-HIP condition of Ti4522XD, at $\sigma_{\max} = 425$ MPa and at 25 °C. The horizontal band of high noise on the right side of (d) is related to an SEM scan error. Due to the high resolution of the DIC procedure, and the large areas mapped, the slip lines appear particularly narrow: the reader is encouraged to view the online version for best resolution and interpretability.

protect the integrity of the Au speckle pattern from thermal exposure for extended periods (> 60 h cumulative).

2.3. Mapping of surface strain

Surface strains were mapped by digital image correlation (DIC) at 25 °C and 670 °C using a remodelled Au speckle pattern applied after EBSD mapping of the unstrained region of interest; this is described more extensively elsewhere [17]. Speckle pattern imaging using back-scattered electrons on a scanning electron microscope (Helios NanoLab, FEI, USA) with optimised imaging conditions as in [15], was performed

across the regions of interest at $4000\times$ magnification using 4096×3536 px² images in a 9×8 tile array, stitched before correlation [23,24]. One may note that grounding work on SEM-DIC [25] indicates that working at higher magnifications, as here, assists in avoiding lens distortion issues: there is a benefit in stitching more, lower resolution, higher magnification images. As such, no spatial distortion correction was applied to the raw images; any remaining spatial distortion was assimilated into the noise threshold for total strain mapping measured. Image correlation of SEM images between the initial, unloaded state, and those acquired at successive cycle interrupts was performed on DaVis software (LaVision, Germany). The

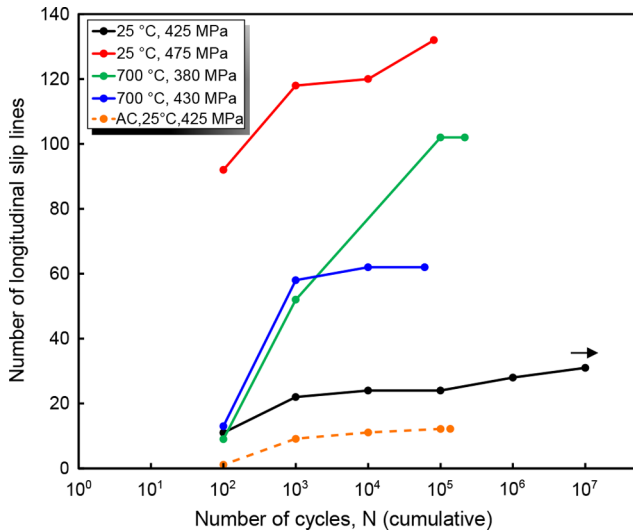


Fig. 4. Evolution in the number of deformation lines during HCF loading. 'AC' refers to the air-cooled, refined lamellar condition; the other four lines correspond to the thicker, as-HIPped lamellar condition. The error in counting, resulting from the 1% maximum shear strain threshold applied, and the operator, is estimated at ± 1 slip line per map: in most cases, this remains low relative to the quantities measured, and in all cases does not affect the trends identified.

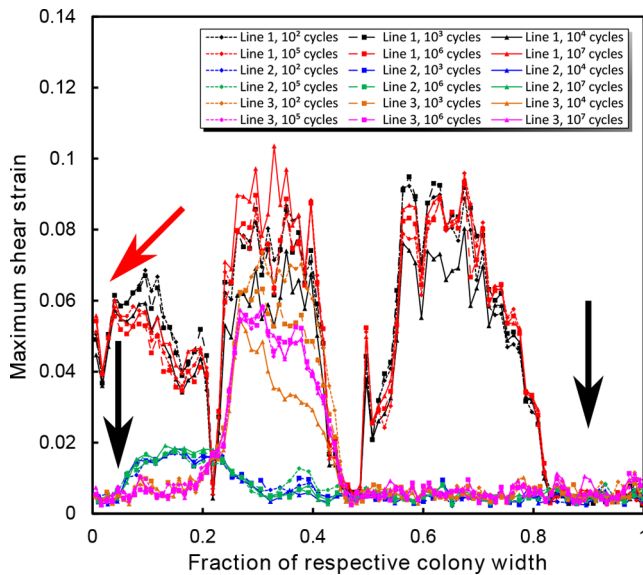


Fig. 5. Lineplots of a selection of the first operative deformation lines numbered in Fig. 3(a) during HCF loading of Ti4522XD at 25 °C and $\sigma_{\max} = 425$ MPa. Black arrows indicate where the shear strain drops to zero by the colony boundary; for the case of line 1 (red arrow), the colony boundary on the left hand side was not within the region of measurement. The error of measurement for the maximum shear strain is 1.8×10^{-3} .

$125 \times 125 \text{ nm}^2$ strain mapping resolution was obtained using a $16 \times 16 \text{ px}^2$ subset size with 25% overlap. The necessity of such resolution to capture localised slip in lamellar TiAl is demonstrated in [15,17]. The noise level in the maximum shear strain of 0.18% for this subset size was measured by correlating repeatedly imaged regions; it resulted from imperfections in SEM raster. DIC strain maps presented here are mapped onto the reference (undeformed) configuration.

Testing was interrupted every factor of ten cumulative cycles from 10^2 cycles to 10^7 cycles. The sample was cooled to room temperature then transferred unloaded to the SEM for pattern imaging, where it was mounted in a bespoke sample holder which mechanically clamped one of the testpiece heads; this significantly reduced the sample drift during

acquisition usually associated with high magnification imaging [25]. The test specimen was then returned to the mechanical test machine and reheated, as initially, to proceed with the next stage of cycling. This test schedule, Fig. 1(c), of repeated sample transfers between test rig and the SEM is equivalent, in essence, to that for LCF testing in [26], however here a factor of $\sim 10^3$ more cycles are achieved. For testing at 670 °C, some test steps were omitted to reduce the total duration of thermal exposure of the Au speckle pattern. The stability of the test parameters during testing is illustrated in the Supplementary Material Fig. S1 of a 9×10^6 cycles loading schedule.

The counting of slip lines was achieved by first applying a 1% maximum shear strain high pass filter; this enabled facile identification of slip lines.

3. Results

3.1. Thick lamellae condition, 25 °C

3.1.1. Thick lamellae condition, 25 °C, $\sigma_{\max} = 425 \text{ MPa}$

The maps of total strain measured by digital image correlation of the surface Au speckle pattern for the successive loading steps for the region of interest in Fig. 2(a,b) of the as-HIPped material condition, loaded in fatigue at 25 °C with $\sigma_{\max} = 425 \text{ MPa}$ and $R = 0.1$, are given in Fig. 3(a–f). After the first 100 loading cycles, ~ 10 micro-slip bands are identified by DIC strain mapping across the complete area of interest. All micro-slip bands lie within soft mode colonies, that is, where the angle ϕ between lamellae and the loading direction lies between 15° and 75° [27,28] (all other lamellar colony orientations are 'hard mode'), and all the bands are longitudinal [13], such that the slip traces are parallel to the lamellar interfaces. The hard-mode colonies remained nominally undeformed. The increase in the number of micro-slip bands with loading cycles is plotted in Fig. 4; this indicator was chosen as it reflects the spatial density of slip initiation events, which may in turn lead to fatigue crack nucleation where incompatibilities at colony (or other) boundaries exist. A selection of lineplots along the first operative micro-slip bands have been extracted, Fig. 5, after each loading interval in Fig. 3, based on pixel locations, which are invariant between steps as the strain maps here are represented in the undeformed geometry. A ten point averaging was employed to smoothen the raw strain mapping data. In nearly all cases, the intensity of the microslip bands diminishes towards the colony boundaries: a shear strain gradient exists. Furthermore, the magnitude of shear strain along the first operative micro-slip bands does not vary noticeably following further test cycles, to within the noise of measurement, Fig. 5. By overlaying the DIC (after 10^7 loading cycles) and EBSD maps, it was possible to locate the micro-slip bands relative to the lamellar structure, Fig. 6. The first operative bands studied were found to locate along γ/α_2 interfaces.

In a few cases a non-zero shear strain was sustained along a micro-slip band up to the colony boundary; in Fig. 7(a), direct longitudinal slip transmission across the colony boundary is impeded as the neighbouring grain is hard-mode oriented. Deformation is seen to deviate along the colony boundary. Upon rotation of the mapping axes to coincide with the micro-slip band and the local tangent to the colony boundary, Fig. 7(b–d), the normal strain component parallel to the colony boundary was below the measurement threshold, whereas the component normal to the boundary reached 5% (tensile); a shear along the colony boundary also exists. This indicates that the longitudinal micro-slip band in the soft-mode colony imposes a mixed mode crack opening stress on the boundary with the hard-mode colony.

The hard TiB₂ particles are not observed to deform; however, where they lie in the path of a longitudinal micro-slip band, local straining is found to deviate along the boride-matrix interface, Fig. 6(a), or halt altogether.

The presence of the Au speckle pattern complicates the identification of surface damage at the successive loading interruptions.

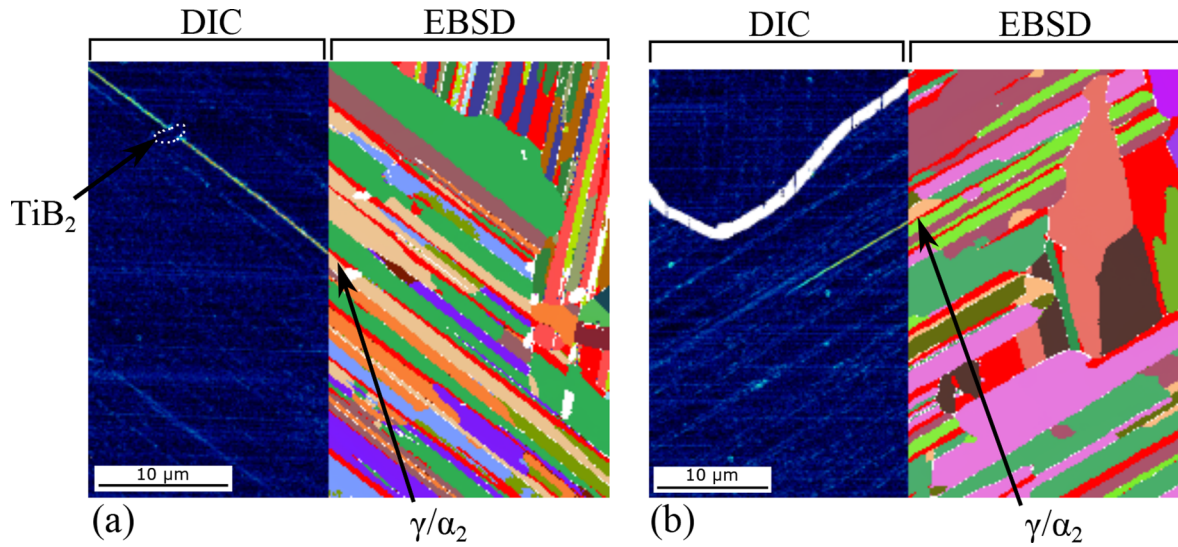


Fig. 6. Combined DIC and EBSD maps to locate the first operative deformation lines. (a) corresponds to line 1 in Fig. 3(a), (b) is line 2 in the same figure.

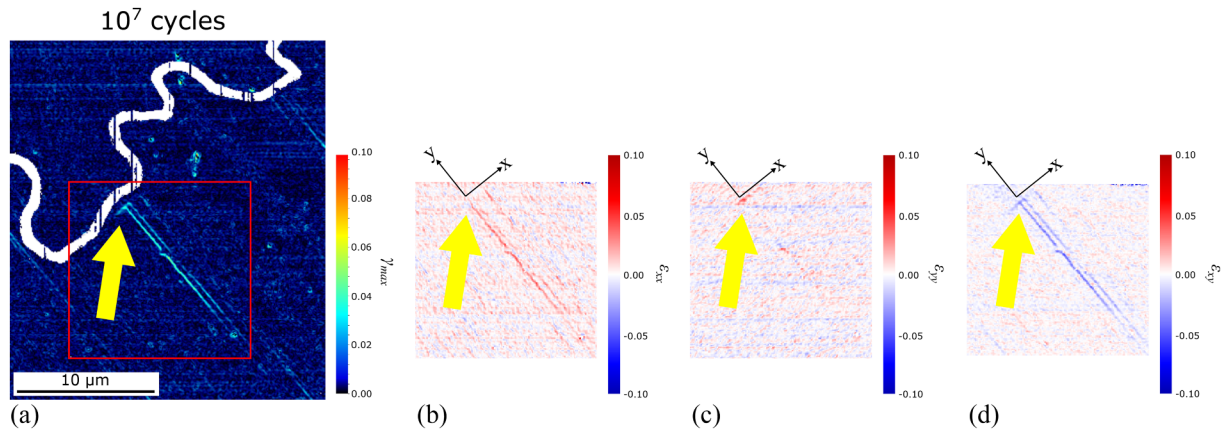


Fig. 7. Detail of the region in the red box in Fig. 3(f); the yellow arrow indicates where a longitudinal slip line in a soft-mode colony is arrested at the colony boundary with a hard-mode colony. Strain is seen to extend laterally, along the colony boundary.

However, several equivalent testpieces were cycled without speckles applied, and without load interruptions, for each test condition, to verify the correct run out at the target $\sigma_{\max,th}$, for example. Supplementary material Fig. S2, a stitched image, constituted of 26 higher resolution SEM images, displays the gauge length of a fatigue testpiece of the thicker lamellar condition ($1.4 \mu\text{m}$ γ -TiAl thickness) that underwent 10^7 cycles at $\sigma_{\max} = 425 \text{ MPa}$, $R = 0.1$ and at 25°C . Indicated as red circles are the locations of fatigue-induced damage (157 total). For the majority ($\sim 70\%$), these crack features lie along colony boundaries, often along the interface with a boride particle, or where an α_2 -Ti₃Al phase lamella meets the colony boundary. The length of such colony boundary crack features was never observed to exceed $10 \mu\text{m}$.

3.1.2. Thick lamellae condition, 25°C , $\sigma_{\max} = 475 \text{ MPa}$

Cyclic loading at 25°C to 50 MPa above the run-out stress, that is to $\sigma_{\max} = 475 \text{ MPa}$, yielded the DIC strain maps in Fig. 8(a–d) for the region of interest in Fig. 2(c,d). The sample failed in the gauge after 81 019 cycles. Again, deformation was focussed in the soft-mode oriented colonies. A significantly increased (8-fold) number of micro-slip bands had developed by 100 loading cycles, relative to the $\sigma_{\max} = 425 \text{ MPa}$ case; however, the proportional increase in the number of new micro-slip bands upon further loading was lower. Again, longitudinal slip bands were found to locate in the vicinity of lamellar

interfaces. Furthermore, although the majority of micro-slip bands still diminished in intensity near colony boundaries, slip transmission was found to occur between longitudinal slip systems across many colony boundaries, as arrowed in orange in Fig. 8(d). The in-plane rotation map for this condition in Fig. 9(b) indicates that the slip lines either side of the colony boundaries in these cases of slip transfer generate compatible deformation, i.e. the rotation from shearing is of the same sign, at least with regards to the plane of study. This differs from the previous condition, Fig. 9(a), where slip lines did generally not even reach the colony boundaries. In addition to the majority of slip operating on longitudinal systems, loading to $\sigma_{\max} = 475 \text{ MPa}$ was found to be sufficient to activate slip on transverse systems [13] in a few hard-mode colonies; these locations are arrowed in pink in Fig. 8(d). Along a small number of the slip lines, the magnitude of shear strain decreased upon further cycling, despite loading being always in tension, e.g. in Fig. 10 of the lines arrowed in yellow in Fig. 8(d).

3.2. Thick lamellae condition, 670°C

3.2.1. Thick lamellae condition, 670°C , $\sigma_{\max} = 380 \text{ MPa}$

Although samples loaded continuously at 670°C without a surface speckle pattern achieved at least 2×10^6 cycles at $\sigma_{\max} = 380 \text{ MPa}$, the sample that underwent several unloading steps for imaging of the speckle only achieved 216 808 cycles. This is likely associated with the

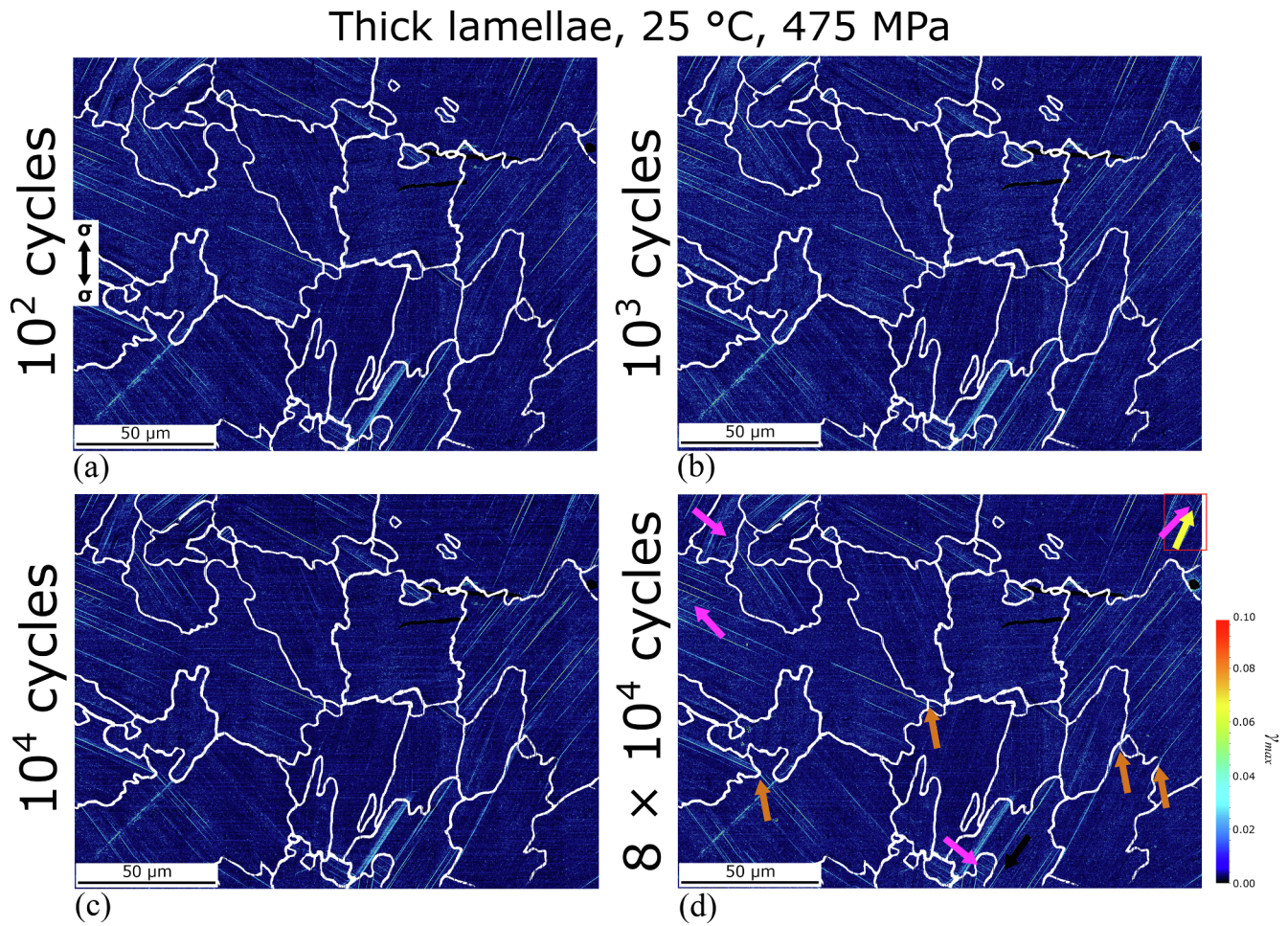


Fig. 8. Maximum shear strain maps for HCF of the as-HIP condition of Ti4522XD, at $\sigma_{\max} = 475$ MPa and at 25 °C. The meaning of the orange, pink and yellow arrows is given in the text. Due to the high resolution of the DIC procedure, and the large areas mapped, the slip lines appear particularly narrow: the reader is encouraged to view the online version for best resolution and interpretability.

experimental difficulty of repeated removal and reinsertion of the sample in the test rig, such that bedding into the grips occurred multiple times. As the duration of high temperature expose increased, the noise in the DIC map above the boride particles, arrowed in white in Fig. 12(c), increased significantly; this is known [17] to be due to reconstruction of the Au speckle on the TiB_2 , rather than a result of their deformation.

Similarly to fatigue loading at $\sigma_{\max, \text{th}}$ at room temperature, deformation at the nominal maximum stress for run-out at 670 °C was exclusively by longitudinal mechanisms, Fig. 12(a – d) of area in Fig. 11(a,b). The number of slip lines, Fig. 4, after 100 loading cycles was found to be similar to that at room temperature at 425 MPa, however at 670 °C the number of slip lines increased more steeply with further cycling, achieving ~ 3 times more by failure than the 425 MPa sample after 10^7 cycles at 25 °C. Strain transfer across colony boundaries by slip transmission was not extensive at 670 °C; one case of apparent slip transmission, arrowed in purple in Fig. 12(c), was found to generate incompatible in-plane rotation, Fig. 13(a), and therefore may only be coincidentally located deformation, rather than slip transmission. Instead, a few regions of localised rotation in the neighbouring colony were identified ahead of slip lines where the magnitude of shear strain did not drop to zero at the colony boundary; these are circled in dashed red lines in the maps of in-plane rotation, Fig. 13. Further, from this rotation map a few longitudinal slip lines are observed to operate in opposite directions of rotation compared to the other slip lines in the same colony, as arrowed in blue in Fig. 13(a); comparison with the map

for the axial strain, ϵ_{yy} , Fig. 14, indicates that both slip line types generate an axial extension. This indicates that within a same colony, deformation on longitudinal systems during HCF at 670 °C occurs in multiple in-plane directions.

3.2.2. Thick lamellae condition, 670 °C, $\sigma_{\max} = 430$ MPa

Loading to $\sigma_{\max} = 430$ MPa at 670 °C produced similar deformation patterns as at lower loads, Fig. 15(a – d) of area in Fig. 11(c,d); by failure, a lesser number of deformation lines were generated in the present region of interest than at $\sigma_{\max} = 380$ MPa. Deformation was again restricted to soft mode colonies, and was always longitudinal.

3.3. Refined lamellae condition

3.3.1. Refined lamellae condition, 25 °C, $\sigma_{\max} = 425$ MPa

Although unspeckled reference samples of the refined lamellae condition achieved 10^7 cycles at $\sigma_{\max} = 425$ MPa at room temperature in continuous loading (no pausing for intermediate unloading), all four attempts at strain mapping at regular intervals, as in Section 3.1.1, saw the semi-brittle intermetallic sample fail below 10^7 cycles, likely due to the repeated removal and reinsertion of the sample in the test rig, causing grip rebidding issues as evoked above. Nevertheless, total strain mapping data could be acquired at $\sigma_{\max} = 425$ MPa and 25 °C until 135 377 cycles, as shown in the Supplementary Material Fig. S4 of the region of interest in Fig. S3. The occurrence of localised plasticity in the refined lamellae condition here is observed to be lesser than for the

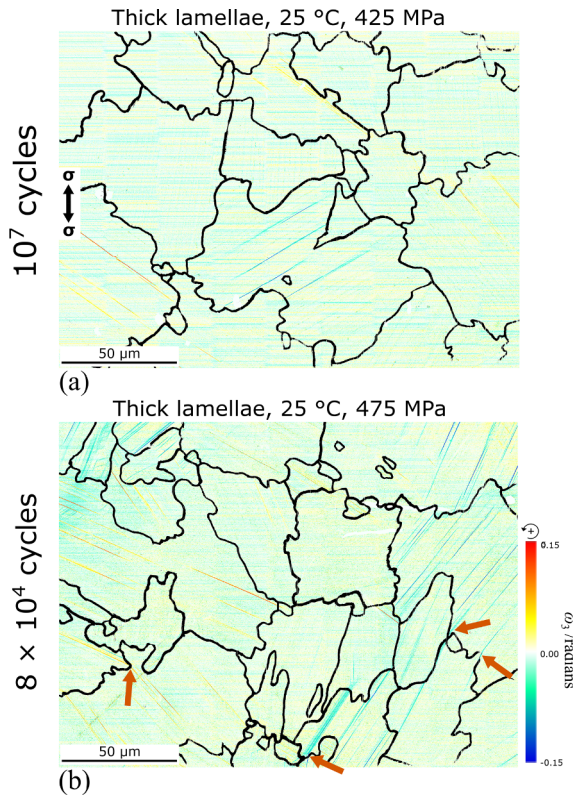


Fig. 9. In-plane rotation maps for HCF of the as-HIP condition of Ti4522XD, at σ_{\max} = (a) 425 and (b) 475 MPa, at 25 °C.

thicker condition above. After 1.4×10^5 cycles, just 12 lines of localised plasticity are measured here, compared to 24 for the previous microstructure at the same test conditions, and a lower cycle count (10^5 cycles), Fig. 4. All such measured localised plasticity was restricted to soft mode colonies, and was always longitudinal. The refinement of the lamellae in this second microstructural condition (160 nm and 50 nm lamellar thicknesses for γ -TiAl and α_2 -Ti₃Al, respectively), and the resolution limitations of EBSD, make association of individual slip lines in the DIC map with certain lamellar interface types impossible from the data presented here.

4. Discussion

In the case of the thicker lamellar microstructural condition (average γ -TiAl thickness: 1.4 μ m), plasticity generated upon high cycle fatigue was found to occur according to similar patterns as for monotonic loading to stresses below the general yield stress [15]:

deformation was almost exclusively longitudinal, occurring only in, and in almost all, soft mode colonies, with small amounts of transverse deformation at higher stresses at room temperature. Consistent with monotonic loading, the first deformation lines were primarily in the vicinity of γ/α_2 interfaces. At 25 °C, the maximum applied stress was found to have a larger impact on the number of slip lines, than the number of cycles applied; the opposite was found at 670 °C: the number of slip lines generated increased significantly as cycling evolved, and similarly so at both maximum stresses applied.

In most cases, the magnitude of shear strain of the slip lines diminished near the colony boundaries, as direct slip transmission across colony boundaries was rare during HCF loading. Further, reverse plasticity was found to exist along some deformation lines at 25 °C as cycling progressed, despite the tension–tension $R = 0.1$ loading; this is presumably due to the local loading state changing as a result of increased plasticity on other systems nearby. It should be noted that little literature was found concerning strain reversal with a non-reversing ($R > 0$) loading schedule as here, and therefore this phenomenon requires further investigation. Indeed, it raises the possibility that between cycling interruptions a minority of slip bands may have nucleated and further seen their strain reversed until a net zero strain is measured: their existence would hence be effectively invisible to the DIC strain measurements at interruption steps. Unlike the monotonic compression in [15], the in-plane rotation generated by longitudinal deformation was not consistently in the same direction per colony: during HCF loading, multiple longitudinal systems must operate in differing slip directions to cause this to occur. It is possible that multiple longitudinal slip directions were operative in other colonies in Fig. 13, however the in-plane rotation from deformation along both directions may have been of the same sign, and therefore the difference in slip direction not captured by surface DIC.

Upon loading at 670 °C, deformation features not observed at room temperature occurred, similarly to during monotonic loading to both below and above the yield stress [14,15]. In particular, the development of regions of rotation ahead of the colony boundaries at the point where a slip line intercepts from a neighbouring colony, as in the dotted red outlined regions of Fig. 13. Features of strain accommodation by localised slip-line gradient-induced lattice rotation have recently [29] been identified as an operative mechanism for lamellar TiAl alloys. The strain levels generated in sub-yield fatigue cycling being relatively low, it is not possible to confirm given the strain resolution of the current DIC strain maps whether the rotation ($1^\circ - 2^\circ$ over a distance of $\sim 5 \mu$ m) is purely elastic lattice rotation, or in fact slip-mediated as in [29].

The boride particles were again found to cause strain to deviate along their interfaces with the matrix, acting as an impassable barrier, similarly as for monotonic loading in [16].

Refinement of the lamellar thickness, from 1.4 μ m down to 160 nm for the γ -TiAl lamellae, resulted in a reduction of the number of active slip lines. Although the strength of this lamellar condition is higher than

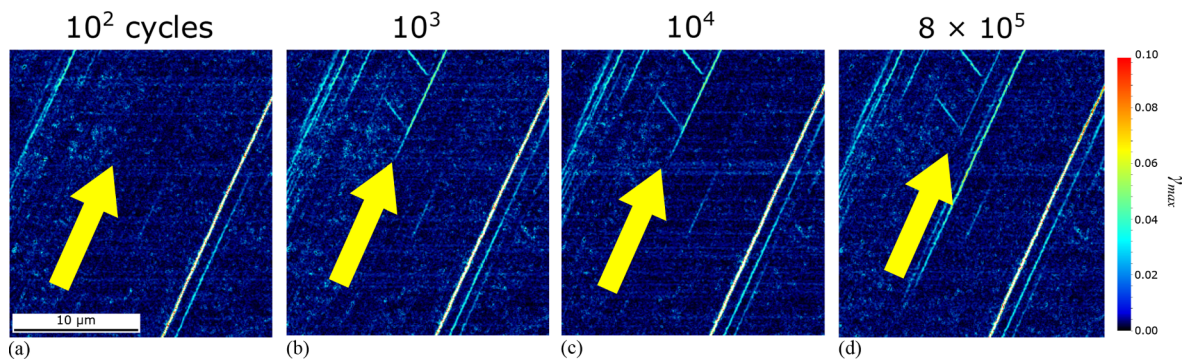


Fig. 10. Strain map sequence of HCF at $\sigma_{\max} = 475$ MPa and 25 °C for the region in the red rectangle in Fig. 8(d); the magnitude of shear strain is found to decrease along the arrowed band with further cycling.

Thick lamellae, 670 °C

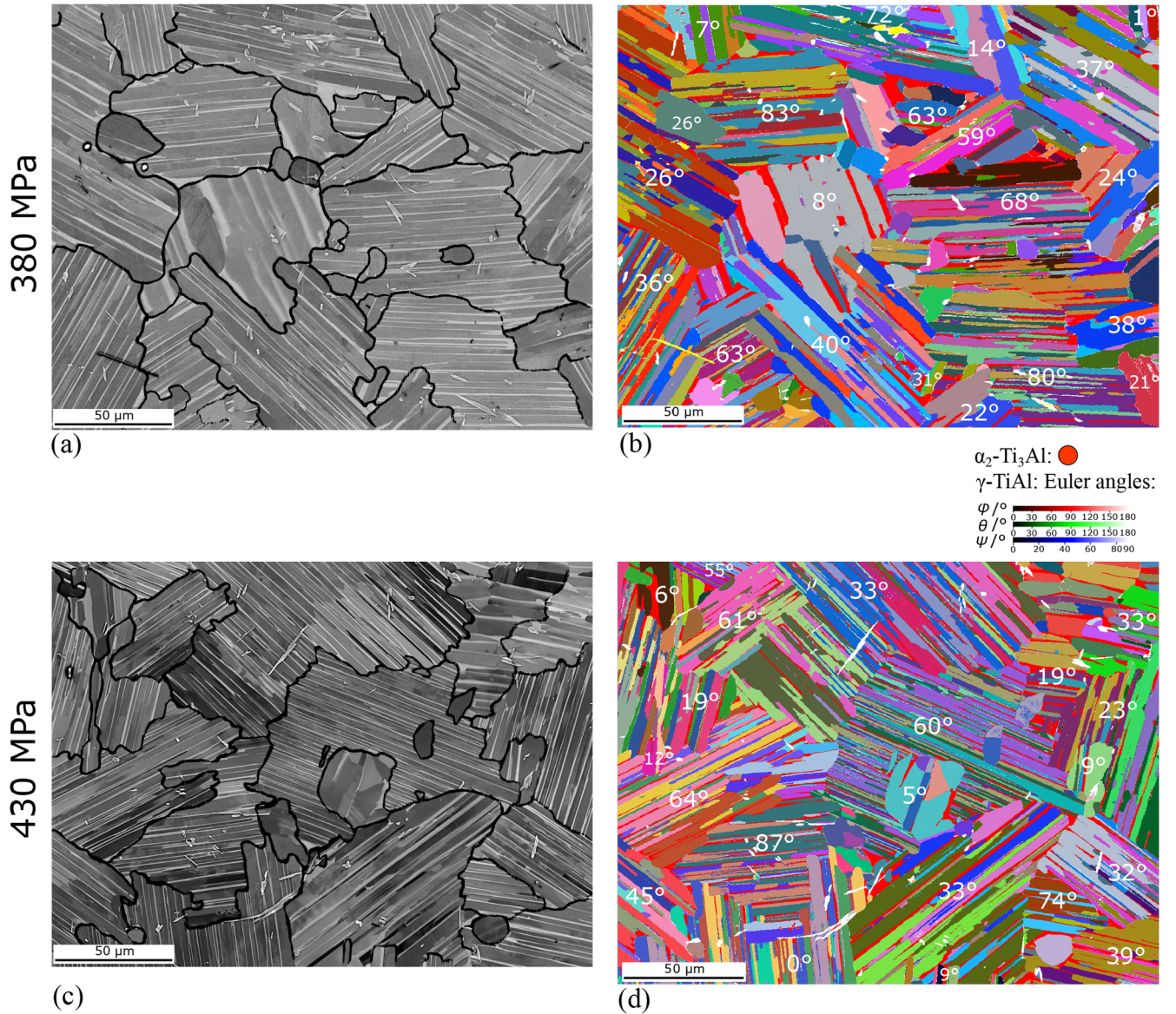


Fig. 11. BSE and EBSD maps of the regions of interest for HCF testing of the as-HIP condition of Ti4522XD at 670 °C. The angle ϕ between the lamellar planes and the loading axis is indicated for each lamellar colony on the EBSD maps.

with thicker lamellae, the decrease in the length of lamellar domains (which may serve to limit the longitudinal plasticity mode) is much lesser than for the lamellar thickness, see Table 2 in [14]. Hence, one may reasonably expect the longitudinal-dominated HCF plasticity to not be substantially affected by the lamellar thickness reduction [14], at least compared to the larger change in the Hall-Petch effect for transverse mode slip; indeed, the yield stress (0.2% strain) in tension at 25 °C, for example, remains unchanged [15], however yielding with refined lamellae is more progressive [14]. From the limited information gleaned into the behaviour of the refined lamellar condition in the present study, it is clear that less distributed plasticity occurs at a same stress than for the thicker lamellae condition, and the material is therefore predicted to be less damage tolerant.

In cases where sample failure occurred below 10^7 cycles at $\sigma_{\max,th}$, repeats of the speckled samples were performed in an attempt to achieve 10^7 cycles without encountering grip bedding issues. Indeed the semi-brittle two-phase intermetallic alloy studied here was found to be particularly susceptible to the removal-reinstallation procedure,

where a tougher alloy may alternatively show some more ductility to accommodate re-bedding in the grips. In general, few repeats of tests were performed due to the complexity of measuring strain maps across relatively large areas, with nanoscale resolution at multiple test intervals upon high cycle fatigue testing at 670 °C, for example. Previous DIC studies by the authors [14,15] with monotonic compressive and tensile loading, where more repeats were performed, indicated that for such an alloy there is good repeatability between samples over an area of $\sim 200 \times 200 \mu\text{m}^2$, covering approximately 25 lamellar colonies, as here.

As discussed in a recent review [5] on the HCF behaviour of TiAl alloys, it may be appropriate to consider the effect on the FCG behaviour of such alloys of such extensive microplasticity as evidenced in the present study occurring over the course of 10^7 loading cycles. Indeed rather than performing FCG measurements on undeformed material to determine the threshold stress intensity factor for design, the above microplasticity could be incorporated as a pre-conditioning step. In fact, one might also note that the majority of the measured

Thick lamellae, 670 °C, 380 MPa

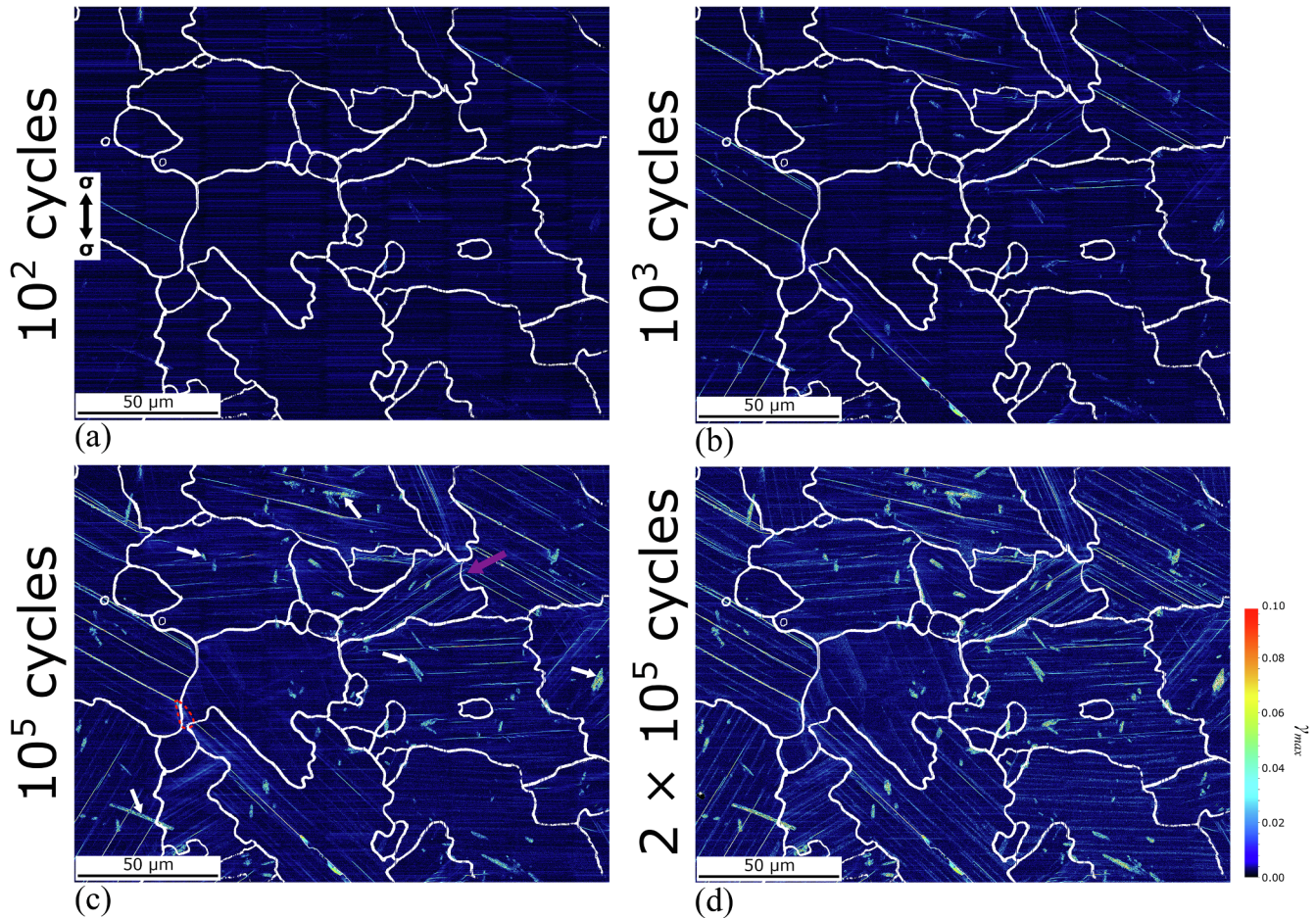


Fig. 12. Maximum shear strain maps for HCF of the as-HIP condition of Ti4522XD, at $\sigma_{\max} = 380$ MPa and at 670 °C. In (c), examples of noise resulting from boride particles exposed at the sample surface are arrowed in white. Due to the high resolution of the DIC procedure, and the large areas mapped, the slip lines appear particularly narrow: the reader is encouraged to view the online version for best resolution and interpretability.

longitudinal slip lines have nucleated after 1000 cycles for most of the experimental conditions here, Fig. 4 (the only exception being 380 MPa, 670 °C, which is arguably the most important from an application viewpoint), and that further the strain within such slip lines does not evolve substantially with further loading cycles after the first sample unloading step following slip line nucleation, Fig. 5. This would suggest that for most test conditions here it may be sufficient to impose only a preconditioning of 1000 fatigue cycles ($R = 0.1$) at a given σ_{\max} to generate a material condition for such alloys that imitates 10^7 cycles ($R = 0.1$) at that same σ_{\max} . The FCG behaviour of such material should then be more representative of the material following several thousands of flights hours expected in service before a crack propagation event should be resisted.

Although equivalent studies of high cycle fatigue with high resolution (i.e. better than standard optical microscopy: SEM, super-resolution optical or AFM-based) DIC strain mapping do not exist on other materials, one may attempt to contextualise the fatigue microplasticity of the lamellar TiAl microstructures of the present study relative to Ni superalloy (René 88DT & RR1000) by referring to recent studies by Stinville et al. [26] and Mello et al. [30] where LCF ($10^3 - 10^4$ times fewer cycles than here) was instead performed, at temperatures up to 650 °C and 700 °C, respectively. Damage in René 88DT was found to surface initiate due to highly localised slip adjacent to growth twin boundaries where the Schmid factor was high and the elastic modulus mismatch along the loading axis direction was greatest. Fully reversed ($R = -1$) fatigue served to create persistent slip bands that mechanically

provided the material required for excessive oxidation along the twin trace at the sample surface, and into the depth along the slip planes. These oxide features eventually fractured, yielding sub-surface cracks. As has been observed in previous studies by the current authors [15], it is thought that the elastic mismatch across lamellar interphase (γ/α_2) boundaries is similarly a cause of strain localisation in TiAl alloys. Although deformation here was not reversed ($R = 0.1$), the observation of strain reversal along a minority of slip lines, Fig. 10, may well provide a mechanism for surface penetrating oxidation at high temperatures in an oxidising atmosphere, as in [26]. In the case of RR1000, for cyclic loading to both strains of 0.7 and 1.0%, the first loading cycle was found to dominate the spatial distribution of strain (slip bands); further cycles simply served to increase the strain within such bands [30]. Increased temperature (300 to 700 °C) and a higher cyclic strain led to a transfer of strain accommodation from octahedral $\{111\}$ slip to cubic $\{100\}$ slip systems, where DIC strain mapping revealed possible simultaneous and extensive activity of both systems within a same grain. This contrasts substantially with lamellar TiAl here: the number of slip lines increases with cycling, whilst the strain within a given line remains generally stable. This indicates that the development of strain upon HCF of this TiAl alloy initially remains highly localised; this may not prove beneficial in limiting damage: highly active $\{111\}$ slip planes in γ -TiAl are known to become easy crack paths [7].

One may note that in [26] the maximum test temperature and cycle count was limited by the deterioration of the native surface oxide used as a speckle pattern. In the present, the overlay Au speckle pattern

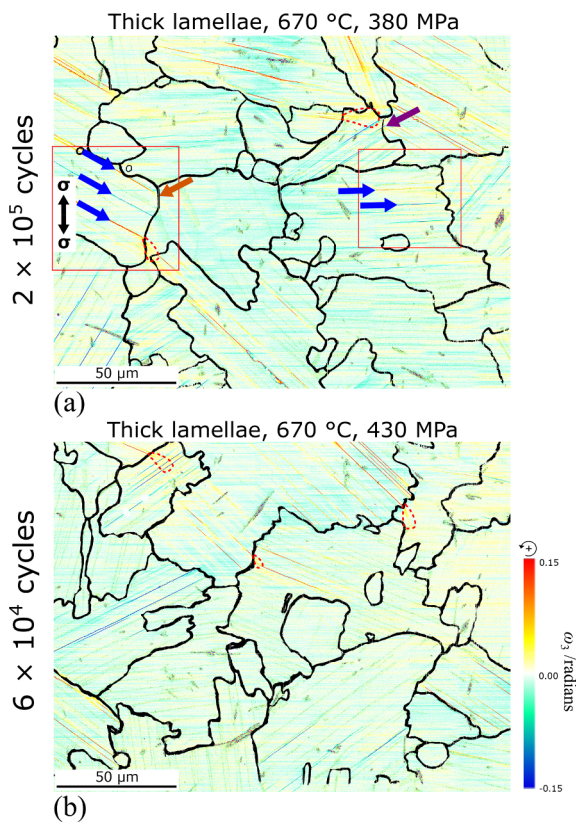


Fig. 13. In-plane rotation maps for HCF of the as-HIP condition of Ti4522XD, at σ_{\max} = (a) 380 and (b) 430 MPa, at 670 °C.

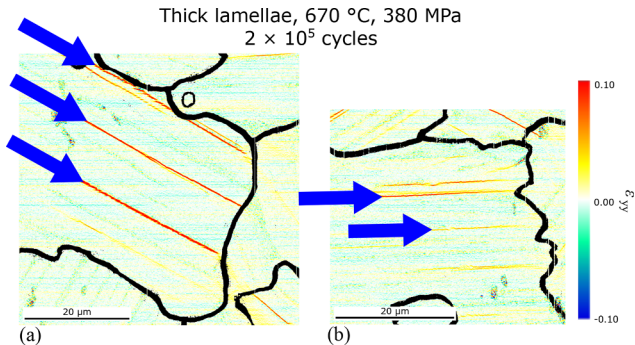


Fig. 14. Axial strain maps for sub-regions in Fig. 13(a).

combined with the higher test frequency (50 vs. 1 Hz in [26]) allowed HCF regime testing to be achieved, but was similarly temperature limited. One might therefore consider a more thermally stable speckle pattern such as a remodelled Pt thin film for more extreme temperatures and test durations [17].

For the samples cycled at $\sigma_{\max,th} + 50$ MPa peak stress, it was unfortunately not possible to effectively capture the initiation of the primary fatigue crack as this did not occur within the regions of interest considered. Indeed, it was not possible to map the total strain throughout the full 6×2 mm² gauge area with sufficiently high (nanoscale) resolution to identify the microstructural features and plasticity patterns. Further, the primary cracks may well have initiated on an alternate face to those mapped by DIC. It is clear that micro-scale testpieces do not provide bulk material properties [15,31]; however, testpieces with intermediate dimensions may well present bulk properties, and maintain a sufficiently reduced gauge area for complete strain mapping. Such *meso*-scale test methods are relatively well established [32], although *in situ* high temperature, high cycle fatigue

testing with the strain mapping instrumentation in the present study has not been demonstrated. A recent study [33] calculated this minimum area for a statistically representative distribution of surface damage in the case of two Ni superalloys (such damage generally nucleated at twin boundaries). For René 88DT, with a grain size of 23 μm , this area was $877 \times 877 \mu\text{m}^2$; whilst for IN100 with 43 μm grains it was $1212 \times 1212 \mu\text{m}^2$. The grain size of the Ti4522XD alloy here is 70 μm . It is complex, however, to extend this to the study of TiAl alloys as not only is there a more than 10-fold increase in the number of growth twin interfaces per grain compared to the Ni superalloys, but the damage mechanisms generally involve colony boundaries (as in Fig. S2 or [16]), rather than the lamellar (twin or interphase) ones. Further, Kad and Asaro [34] have shown that too small a sample size relative to the lamellar colony size significantly reduces the strength of the testpiece. In short, to apply a strain mapping method across the full gauge section of a lamellar TiAl HCF testpiece with bulk-like properties, with sufficient resolution to resolve the plasticity of individual lamellae, and within a reasonable test timescale, a finer colony size must be sought. The colony sizes of 3rd generation alloys (e.g. TNM, TNBv4 [35]) are generally optimised to 50 μm or below, i.e. lower than their 2nd generation counterparts. Such 3rd generation alloys are therefore a promising candidate for further strain mapping studies to analyse the fatigue failure initiation of TiAl alloys, and the effect of the additional softer β -TiAl phase, which locates along colony boundaries, on the accommodation of strain between the lamellar colonies, which are known from the previous studies by the authors to be of considerably variable, and often incompatible, deformability.

The present DIC study provides quantitative information on the nano-to-micro-scale distribution of plasticity in lamellar TiAl during high cycle fatigue, in application-relevant conditions at and above the threshold stress for run-out. Such data could not be obtained by alternative experimental methods: standard post-mortem microscopy techniques (bulk surface or transmission) are unable to capture the proportionate activity of different deformation systems, *in situ* TEM loading where active dislocations may be counted has too limited a field of view to capture the spatial wavelength of dominant localised strain here, whilst diffraction methods using X-rays or neutrons are limited to elastic and volume-integrated plasticity data. The present dataset aids both the understanding of high cycle fatigue damage in current TiAl material, and in the design of advanced TiAl alloys for increased damage tolerance through microstructural design, whereby a more uniform distribution of microplasticity, accommodated by effective strain transfer at microstructural boundaries, is to be targeted – similarly to current industrial awareness of twin-boundary-induced LCF failure in Ni superalloys, an issue identified in parallel DIC studies [26].

5. Conclusions

The high cycle fatigue behaviour of polycrystals of Ti-45Al-2Nb-2Mn(at%)-0.8 vol% TiB₂ was investigated at both 25 °C and 670 °C, with interrupted and resumed cyclic loading to enable image acquisition for total strain mapping. Exclusively longitudinal plasticity occurred in most colonies with soft mode lamellar orientations and was located near lamellar interfaces. In most cases, plastic strains decreased to zero by the colony boundary; strain transfer across such boundaries in high cycle fatigue was rare at all temperatures investigated. At room temperature, the maximum applied stress was found to influence the number of slip bands more so than did the number of loading cycles.

Declaration of Competing Interest

The authors declare that they have no known competing financial interests or personal relationships that could have appeared to influence the work reported in this paper.

Thick lamellae, 670 °C, 430 MPa

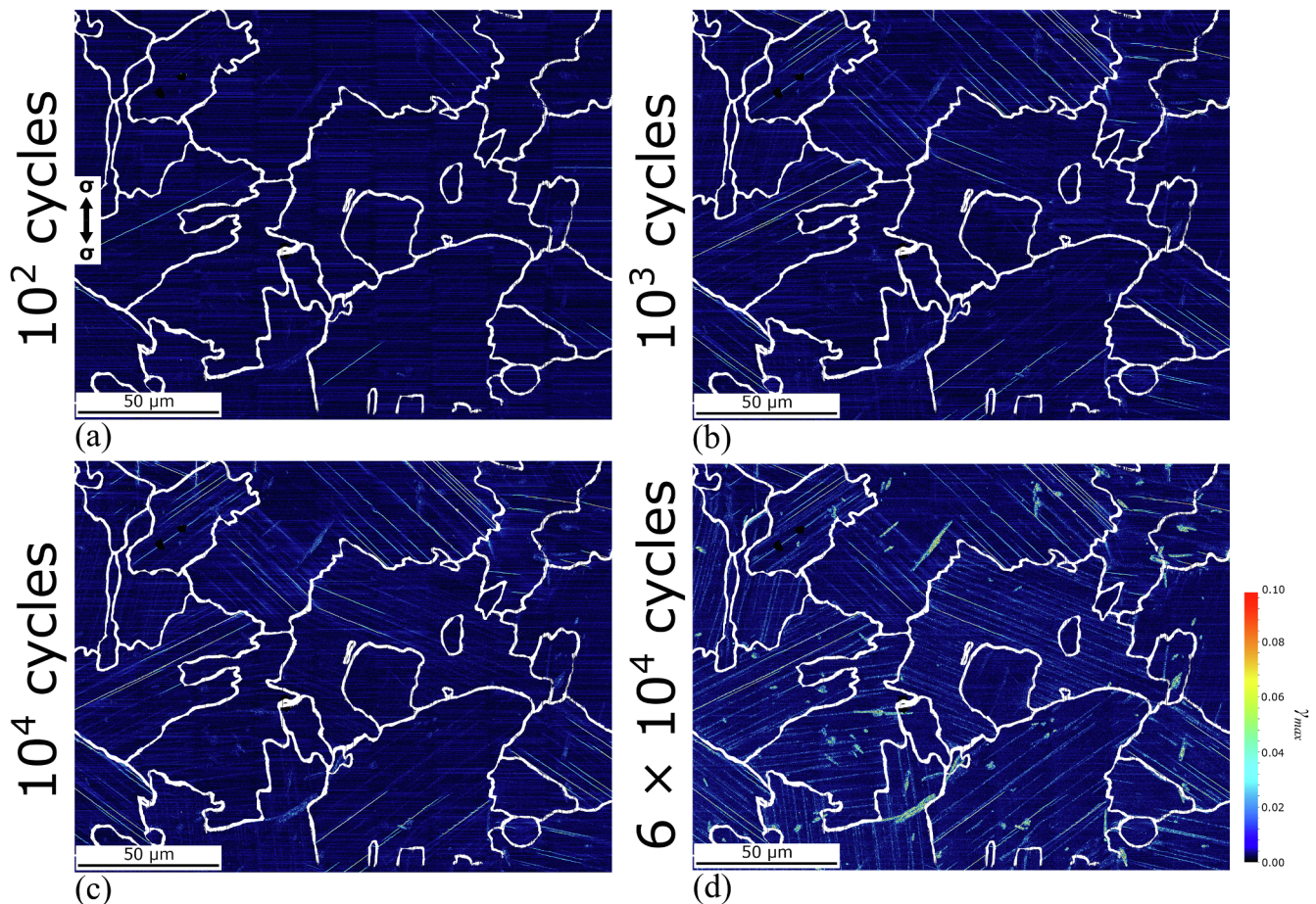


Fig. 15. Maximum shear strain maps for HCF of the as-HIP condition of Ti4522XD, at $\sigma_{\max} = 430$ MPa and at 670 °C. Due to the high resolution of the DIC procedure, and the large areas mapped, the slip lines appear particularly narrow: the reader is encouraged to view the online version for best resolution and interpretability.

Acknowledgements

The work was supported by the EPSRC / Rolls-Royce Strategic Partnership (EP/M005607/1). T.E.J.E. also acknowledges the kind support of the Worshipful Company of Armourers and Brasiers' Gauntlet Trust, and the EMPAPOSTDOCS-II programme which has received funding from the European Union's Horizon 2020 research and innovation programme under the Marie Skłodowska-Curie grant agreement number 754364.

Appendix A. Supplementary data

Supplementary data to this article can be found online at <https://doi.org/10.1016/j.ijfatigue.2020.105905>.

References

- [1] Bewlay BP, et al. TiAl alloys in commercial aircraft engines. *Mater High Temp* 2016;33(4–5):549–59.
- [2] Goold I. Rolls-Royce Advances Toward UltraFan; 2014.
- [3] Tetsui T, Miura Y. Heat-resistant cast TiAl alloy for passenger vehicle turbochargers. *Mitsubishi Heavy Industries Tech Rev* 2002;39(1):200.
- [4] Zhu H, et al. Assessment of titanium aluminide alloys for high-temperature nuclear structural applications. *JOM* 2012;64(12):1418–24.
- [5] Edwards TEJ. Recent progress in the high-cycle fatigue behaviour of γ -TiAl alloys. *Mater Sci Technol* 2018:1–21.
- [6] Rugg D, Dixon M, Burrows J. High-temperature application of titanium alloys in gas turbines. *Material life cycle opportunities and threats – an industrial perspective*. *Mater High Temp* 2016;33(4–5):536–41.
- [7] Appel F, Paul JDH, Oehring M. Gamma titanium aluminide alloys : science and technology. 2011, Weinheim: Wiley-VCH. xvi, 745 p.
- [8] Larsen J, et al. Assuring reliability of gamma titanium aluminides in long-term service. *Miner, Metals Mater Soc/AIME, Gamma Titanium Aluminides* 1999;1999(USA):463–72.
- [9] Niendorf T, et al. Early detection of crack initiation sites in TiAl alloys during low-cycle fatigue at high temperatures utilizing digital image correlation. *Int J Mater Res* 2009;100(4):603–8.
- [10] İçöz C, et al. Strain accumulation in TiAl intermetallics via high-resolution digital image correlation (DIC). *Procedia Eng* 2014;74:443–8.
- [11] Patriarca L, Filippini M, Beretta S. Digital image correlation-based analysis of strain accumulation on a duplex γ -TiAl. *Intermetallics* 2016;75:42–50.
- [12] Bode B, et al. Local deformation at micro-notches and crack initiation in an intermetallic γ -TiAl-alloy. *Fatigue Fract Eng Mater Struct* 2016;39(2):227–37.
- [13] Lebensohn R, et al. Plastic flow of γ -TiAl-based polysynthetically twinned crystals: micromechanical modeling and experimental validation. *Acta Mater* 1998;46(13):4701–9.
- [14] Edwards TEJ, Di Gioacchino F, Clegg WJ. An experimental study of polycrystalline plasticity in lamellar titanium aluminide. *Int J Plast* 2019;118.
- [15] Edwards TEJ, et al. Deformation of lamellar γ -TiAl below the general yield stress. *Acta Mater* 2019;163:122–39.
- [16] Edwards TEJ et al., The interaction of borides and longitudinal twinning in polycrystalline TiAl alloys. *Acta Materialia*, 2017. 140(Supplement C): p. 305–316.
- [17] Edwards TEJ, et al. Stable speckle patterns for nano-scale strain mapping up to 700 °C. *Exp Mech* 2017;57:1289–309.
- [18] Chen L, et al. Crystal plasticity analysis of deformation anisotropy of lamellar TiAl alloy: 3D microstructure-based modelling and in-situ micro-compression. *Int J Plast* 2019;119:344–60.
- [19] Edwards TEJ, et al. Transverse deformation in a lamellar TiAl alloy at high temperature by in situ microcompression. *Acta Mater* 2019;166:85–99.
- [20] Edwards TEJ, et al. Longitudinal twinning in a TiAl alloy at high temperature by in situ microcompression. *Acta Mater* 2018;148:202–15.
- [21] Edwards TEJ, et al. Deformation of lamellar TiAl alloys by longitudinal twinning. *Scr Mater* 2016;118:46–50.
- [22] Edwards TEJ, et al. Slip bands in lamellar TiAl during high cycle fatigue micro-compression by correlative total strain mapping, diffraction orientation mapping

- and transmission electron imaging. *Int J Fatigue* 2019;124.
- [23] Preibisch S, Saalfeld S, Tomancak P. Globally optimal stitching of tiled 3D microscopic image acquisitions. *Bioinformatics* 2009;25(11):1463–5.
- [24] Schindelin J, et al. Fiji: an open-source platform for biological-image analysis. *Nat Meth* 2012;9(7):676–82.
- [25] Kammers AD, Daly S. Digital image correlation under scanning electron microscopy: methodology and validation. *Exp Mech* 2013;53(9):1743–61.
- [26] Stinville JC, et al. Measurement of strain localization resulting from monotonic and cyclic loading at 650 °C in nickel base superalloys. *Exp Mech* 2017;57:1469–82.
- [27] Fujiwara T, et al. Deformation of polysynthetically twinned crystals of TiAl with a nearly stoichiometric composition. *Philos Mag A* 1990;61(4):591–606.
- [28] Inui H, et al. Room-temperature tensile deformation of polysynthetically twinned (PST) crystals of TiAl. *Acta Metall Mater* 1992;40(11):3095–104.
- [29] Di Gioacchino F, et al. A new mechanism of strain transfer in polycrystals. *Sci Rep* 2020;10(1):10082.
- [30] Mello AW, Nicolas A, Sangid MD. Fatigue strain mapping via digital image correlation for Ni-based superalloys: The role of thermal activation on cube slip. *Mater Sci Eng, A* 2017;695:332–41.
- [31] Palomares-García AJ, Pérez-Prado MT, Molina-Aldareguia JM. Slip transfer across γ -TiAl lamellae in tension. *Mater Des* 2018;146:81–95.
- [32] Legros M, et al. Microsample tensile testing of nanocrystalline metals. *Philos Mag A* 2000;80(4):1017–26.
- [33] Stinville JC, et al. Microstructural statistics for fatigue crack initiation in polycrystalline nickel-base superalloys. *Int J Fract* 2017;208(1):221–40.
- [34] Kad BK, Asaro RJ. Apparent Hall-Petch effects in polycrystalline lamellar TiAl. *Philos Mag A* 1997;75(1):87–104.
- [35] Clemens H, Mayer S. Alloy design criteria for advance titanium aluminides. In *IWTA2016*. 2016. Tokyo, Japan.